Direct numerical simulation of Taylor–Couette turbulent flow controlled by a traveling wave-like blowing and suction

K. Ogino[a], H. Mamori[b,*], N. Fukushima[c], K. Fukudome[a], M. Yamamoto[a]

[a] *Department of Mechanical Engineering, Tokyo University of Science, 6-3-1 Niijuku, Katsushika, Tokyo 125-8585, Japan*
[b] *Department of Mechanical and Intelligent Systems Engineering, The University of Electro-Communications, 1-5-1, Chofugaoka, Chofu, Tokyo 182-8585, Japan*
[c] *Department of Prime Mover Engineering, Tokai University, 4-1-1, Kitakaname, Hiratsuka, Kanagawa, 259-1292, Japan*

Abstract

In wall turbulence, a traveling wave-like control is known to decrease the skin-friction drag and induce the relaminarization phenomenon. Because it is noteworthy to investigate the control effect in other canonical flows, direct numerical simulations of fully developed turbulent Taylor–Couette flows are performed. The Reynolds number, based on the wall velocity of a rotating inner cylinder and the radius of a centerline between cylinders, is set to 84,000. The traveling wave-like blowing and suction is imposed on the inner or outer cylinder wall, and the control effect is parametrically investigated. In the inner cylinder control, the torque reduction is obtained when the wave travels in the co-rotating direction with the inner cylinder, and its wavespeed is faster than the rotation. In the outer cylinder control, in contrast, the torque reduction is obtained when the wave propagates in the opposite direction. While the control is imposed on one side wall (i.e., inner or outer cylinder), the control affects the entire flow region. The Taylor vortex remains, while the traveling wave affects its strength. The three-component decomposition analysis shows that the traveling wave creates the coherent contribution on the torque, while the random contribution on

*Corresponding author
Email address: mamori@uec.ac.jp (H. Mamori)

it is reduced. Accordingly, a major factor of the torque reduction in the Taylor–Couette flow is the reduction of the random contribution. In addition, for the faster wavespeed cases with the small wavenumber (i.e., the long wavelength), the drag reduction larger than 60% is obtained and the relaminarization occurs in these cases.

Keywords: Taylor–Couette flow, torque reduction, traveling wave control, direct numerical simulation

2016 MSC: 00-01, 99-00

1. Introduction

In wall turbulence, skin-friction drag is known to increase the energy losses and there are many control techniques aiming to decrease it. Furthermore, the skin-friction drag in wall turbulence significantly increases owing to the quasi-streamwise vortical structures. The identity equation of the skin-friction coefficient c_f [1] in a fully developed turbulent channel flow is written as follows:

$$c_f = \frac{12}{\mathrm{Re}} + 12 \int_0^1 2(1-y)(-\overline{u'v'})dy, \tag{1}$$

where the first and the second terms are the contributions from the laminar and the turbulent flow, respectively. The turbulent contribution term is the integration of the y-weighted Reynolds shear stress ($-\overline{u'v'}$), which corresponds to the activity of the quasi streamwise vortical structure.

Based on Eq. (1), Min *et al.* [2] performed the traveling wave-like blowing and suction control in a fully developed turbulent channel flow, the traveling wave decreases the skin-friction drag when the wave travels in the upstream direction. Subsequently, the traveling wave, which stabilizes the flow [3], can be used to control the onset of transition [4, 5] and induce a relaminarization phenomenon with positive efficiency [6, 7]. In addition, the wave control demonstrates the heat transfer enhancement effect [8, 9]. While Xu *et al.* [10] used the traveling wave to suppress the vortex vibration of a circular cylinder, many studies for the traveling wave control are carried out in the Poiseuille flows as reviewed above.

In the present study, direct numerical simulations (DNSs) of turbulent Taylor–Couette flows controlled by the traveling wave-like blowing and suction are performed. Taylor [11] was the first to study the flow between the two cylinders (i.e., so-called the Taylor–Couette flow and referred as the TC flow hereafter) and defined the Taylor vortex. Andereck [12] made an experimental study to categorize the flow pattern of the TC flow. When the inner cylinder is fixed or is slowly rotating, the TC flow is linearly stable for the outer cylinder rotation; as the rotational velocity of the inner cylinder increases, the onset of instability is caused and various flow patterns appear, e.g., Taylor vortex, modulated waves, spirals etc. The Taylor–Couette flow changes its flow pattern with the increase of the Reynolds number [13, 14, 15, 16]. Quasi-periodicity in the azimuthal direction has been found in weakly turbulent states, which disappears for higher Reynolds number cases [17, 18].

The torque and the scaling exponent α, defined by the dimensionless torque $G \propto \mathrm{Re}^{\alpha}$, have been measured in many experimental studies on Taylor–Couette flow with a rotating inner cylinder [15, 16, 19, 20]. The Reynolds number dependence on the mean torque at the inner cylinder shows a transition at $\mathrm{Re} \approx 10,000$ [15, 16], where Re is based on the gap width and the rotating speed of inner cylinder.

Recently, DNSs of the turbulent Taylor–Couette flow have been conducted to investigate its statistical and dynamical features [21, 22, 23]. DNSs of the Taylor–Couette flow have been also carried out for $\mathrm{Re} = 2,000 \sim 12,000$ to clarify the turbulence transition and characteristics of fine scale eddies in a turbulent Taylor–Couette flow. While fine scale eddies are formed in a stepwise fashion with the increase of Reynolds number, large scale Taylor vortices still persist even for the highest Reynolds number case [24]. Osawa *et al.* [25] conducted DNSs of Taylor–Couette flow from $\mathrm{Re} = 8,000$ to $25,000$ to investigate the transition of turbulence statistics in a wide range of Reynolds numbers. Fukushima *et al.* [26] performed DNSs to clarify the turbulence transition and dynamic characteristics of large vortical structures and fine scale eddies. In addition, the turbulent transition can occur in supercritical or subcritical state

depending on which cylinder is rotated [27].

The TC flow is one of the canonical flows. However, it is different from the Poiseuille flow, e.g., the Taylor vortex appears, the driving force is the wall velocity, there is a wall curvature, and the TC flow has many modes depending on the parameters [28]. As a passive control technique, Watanabe and Akino [29] experimentally investigated the drag reduction effect of the laminar TC flow by a highly water-repellent wall. Greidanus *et al.* [30] experimented on the turbulent TC flow on a cylinder with riblet surfaces and obtained 3.4% drag reduction. As an active control technique, Le Dauphin and Fukagata [31] performed the DNS of a Taylor–Couette flow with opposition control. The opposition control [32] is one of the feedback control techniques where the blowing and suction from the wall is imposed to cancel the activity of the vortical structures. It is based on detecting the velocity in the region near the wall. In addition, Le Dauphin and Fukagata [31] confirmed 31.5 % of the torque reduction effect by a combination of the wall-normal and the azimuthal velocities from the wall surface.

The objective of this study is to investigate the torque reduction effect by the traveling wave-like blowing and suction in the TC flow by using DNSs. In the present TC flow, only the inner cylinder is rotating and the traveling wave is imposed on the inner or outer cylinders. The control effect is parametrically investigated.

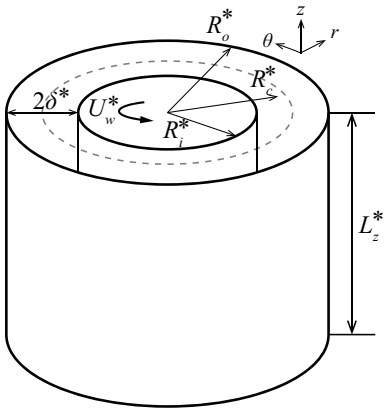

Figure 1: Schematic of Taylor–Couette flow and coordinate systems.

2. Direct Numerical Simulation

The Taylor–Couette flow is displayed in Fig. 1. The inner cylinder is rotating with a wall velocity of U_w^* and the outer cylinder is immobile. An inner cylinder radius is denoted by R_i^* and an outer one by R_o^*. Consequently, a centerline between two cylinders is located at $R_c^* = (R_i^* + R_o^*)/2$ and the half width of the gap is $\delta^* = (R_o^* - R_i^*)/2$. The dimensionless inner and outer radii are $R_i^*/R_c^* = 0.937$ and $R_o^*/R_c^* = 1.06$, respectively. A ratio between the inner and outer cylinder radii is set to be $\xi = R_i^*/R_o^* = 0.882$. The asterisk denotes dimensional variable. In this paper, U_w^* and R_c^* are employed as the reference velocity and length, respectively, and the coordinates and the velocities are made dimensionless by them.

A periodic condition has been imposed in the axial direction and a no-slip condition has been imposed on the wall. The governing equations are an incompressible continuity equation and a Navier–Stokes equations in a cylindrical coordinate system. The Reynolds number defined by U_w^* and R_c^* is set to be $\mathrm{Re}_c = 84,000$. The computational length in the z-direction is $L_z = 5\delta$ and the computational grid points are $N_r \times N_\theta \times N_z = 128 \times 512 \times 256$. In this computational domain, the Taylor vortex appears as discussed later. While the length

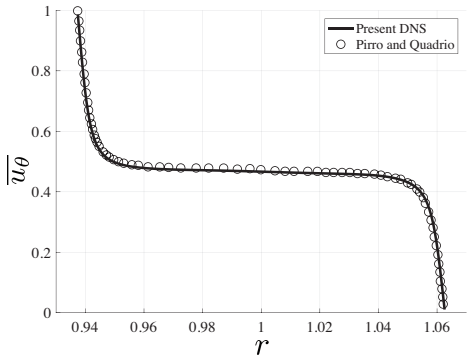

Figure 2: The mean azimuthal velocity as compared with Pirró and Quadrio [23].

in z-direction is short as compared with ordinary simulation for Taylor-Couette flow, this length is chosen to reduce the computational cost for the parametric study. All simulations start from the fully developed TC flow of $\mathrm{Re}_c = 84,000$. The flow field was calculated using a direct numerical calculation code discretized by the energy conservative finite difference method [33]. A staggered grid system is employed: the pressure is defined at the center of the cell, while velocities are defined on the face of the cells. The mesh size is uniform in the axial and azimuthal directions and is non-uniform in the wall-normal direction.

Figure 2 shows the mean azimuthal velocity $\overline{u_\theta}$ in the uncontrolled TC flow. The bar denotes the temporal and spatial (in z- and θ- directions) average:

$$\overline{f}(r) = \frac{1}{\mathscr{T} 2\pi L_z} \int_0^{\mathscr{T}} \int_0^{2\pi} \int_0^{L_z} f dz d\theta dt, \tag{2}$$

where f is an arbitrary and $\mathscr{T}$ is an averaging time. The fluctuation from the temporal and spatial (in z- and θ- directions) average is denoted by the prime, i.e., $f = \overline{f} + f'$. As shown in Fig. 2, the mean azimuthal velocity in the present case is in agreement with the statistics by Pirró and Quadrio [23].

Figure 3 shows the schematic of a traveling wave-like blowing and suction on the wall. The traveling wave is given as:

$$u_{r,w} = a \sin(k(\theta - ct)). \tag{3}$$

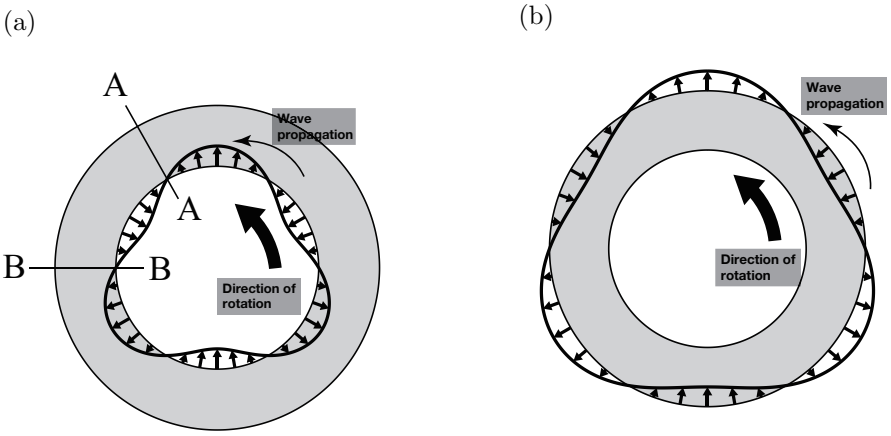

Figure 3: Top view of the traveling wave on (a) the inner wall and (b) outer wall.

Table 1: Range of control parameters.

	a	k	c
Inner control	0.01, 0.1, 0.2	1, 2, 3, 5, 10	± 0.94, ± 1.88, -4.7, ± 7.52, ± 9.4
Outer control	0.1, 0.2	1, 2, 3, 5, 10	± 1.06, ± 2.12, -5.3, ± 8.64, ± 10.6

Here, $u_{r,w}$ is the wall-normal velocity on the wall, a is the amplitude of the wave, k is the wavenumber, and c is the wave speed. The thin arrows indicate the traveling direction of the wave. A positive c means that the wave rotates in the same direction of the inner cylinder rotation. Figure 3(a) is the schematic of an inner cylinder control case (i.e., the wave is imposed on the inner cylinder) and "A-A" and "B-B" are visualized planes in the following section. Figure 3(b) is an outer cylinder control. The control effect is investigated for 63 cases in the inner control and 54 cases in the outer control. The range of control parameters is tabulated in Table 1.

The present DNS is compared with data obtained using a larger domain size and a finer mesh. Table 2 shows numerical parameters, where 'NC' and 'CTRL' indicate no control and control (i.e., traveling wave), respectively. NC-ref and CTRL-ref represent numerical parameters employed in the present study. NC-

Table 2: Numerical parameters for verification.

Case	L_z	$(N_r \times N_\theta \times N_z)$	control input	(a, k, c)
NC-ref	5δ	$(128 \times 512 \times 256)$	$--$	$--$
NC-extend	10δ	$(128 \times 512 \times 512)$	$--$	$--$
CTRL-ref	5δ	$(128 \times 512 \times 256)$	inner control	$(0.1, 3, 9.4)$
CTRL-extend	10δ	$(128 \times 512 \times 512)$	inner control	$(0.1, 3, 9.4)$
CTRL (r-fine)	5δ	$(256 \times 512 \times 256)$	inner control	$(0.1, 3, 9.4)$
CTRL (θ-fine)	5δ	$(128 \times 1024 \times 256)$	inner control	$(0.1, 3, 9.4)$
CTRL (z-fine)	5δ	$(128 \times 512 \times 512)$	inner control	$(0.1, 3, 9.4)$

extend and CTRL-extend employ a computational domain of double the length in the z-direction with the same resolution as NC-ref and CTRL-ref. CTRL (r-fine), CTRL (θ-fine), and CTRL (z-fine) use fine computational meshes in r-, θ-, and z-directions, respectively.

Figure 4 compares the statistics of the uncontrolled and controlled flows with different computational domains. The small difference is observed. However, the torque reduction rates of the uncontrolled and controlled flows are 27 % and 25 % in $L_z = 5\delta$ and $L_z = 10\delta$, respectively. Figure 5 shows the statistics of the controlled flow for different computational meshes. The statistics in CTRL-ref well agree those in the finer mesh cases. Accordingly, the controlled flow can be reproduced by the reference computational domain and resolution despite the short length in the z-direction.

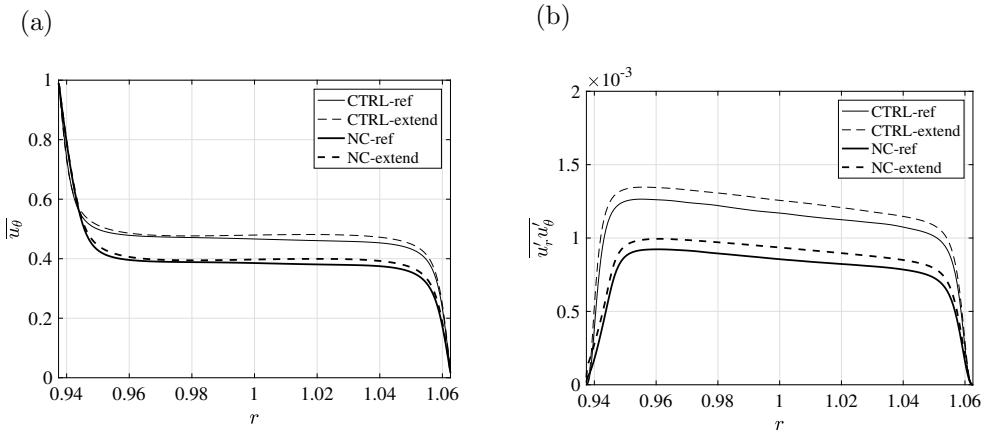

Figure 4: Domain side dependency on the statistics of the uncontrolled and controlled flows (a) $\overline{u_\theta}$ and (b) Reynolds shear stress $\overline{u_r' u_\theta'}$.

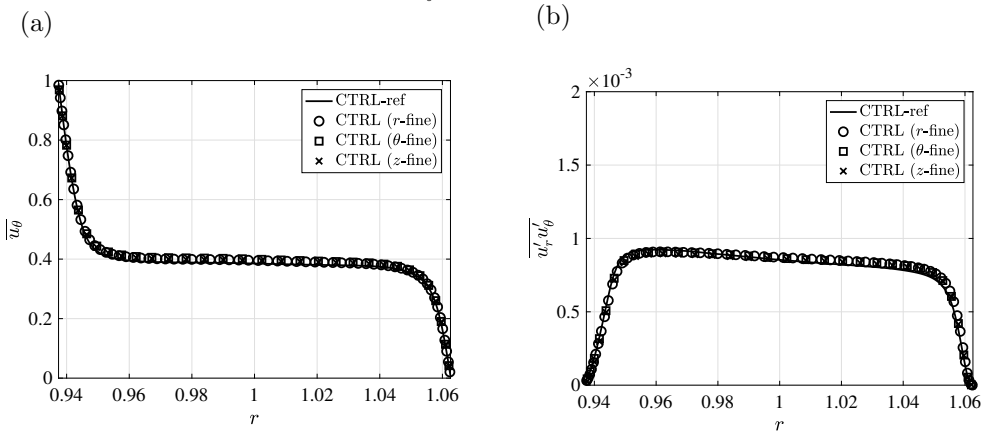

Figure 5: Grid number dependency on the statistics of the controlled flow (a) $\overline{u_\theta}$ and (b) Reynolds shear stress $\overline{u_r' u_\theta'}$.

3. Results and Discussion

The control effect is discussed by using a torque reduction rate R_T defined as,

$$R_T = \frac{T_{nc} - T}{T_{nc}} \times 100[\%]. \tag{4}$$

The subscript of nc is the uncontrolled case and the dimensionless torque T is defined as,

$$T = 2\pi R_i L_z \, R_i \left. \frac{\partial \overline{u_\theta}}{\partial r} \right|_{i,w}, \tag{5}$$

where $\left(\partial \overline{u_\theta}\right)/\partial r|_{i,w}$ is the mean velocity gradient on the inner wall surface. The torque T is balanced with the one on the outer cylinder.

Figure 6(a) shows a map of R_T by the inner cylinder control as a function of c and k at $a = 0.1$. The positive torque reduction rate $R_T > 0$ is obtained at $c > 3.2$, which indicates that a co-rotating traveling wave reduces the torque when the wave is faster than the rotation of the inner cylinder. The drag reduction rate larger than 20% is obtained at $k = 1$ and 2 with $c > 1.6$. Moreover, in the faster traveling wave case at $c > 7.52$ with $a = 0.1$ and $k = 1$, the large torque reduction rate ($R_T > 60\%$) is obtained and the relaminarization phenomenon occurs in these parameter sets. The effect of a is shown in Fig. 6(b). Positive R_T is obtained at $c > 3.2$ and it increases with the increase of a.

A map of R_T in the outer cylinder control is shown in Fig. 7. In contrast to the inner cylinder control, the torque reduction is obtained with negative wave speed of $c < -1.4$, except for small wave numbers (i.e., $k = 1$ with $c = -1.4$ and $c = -2.8$). In this case, the negative wave speed corresponds to the counter-rotation of the inner cylinder rotation. As shown in Fig. 7b, the torque reduction rate of $a = 0.2$ is larger than that of $a = 0.1$. Additionally, the relaminarization phenomenon occurs in the faster traveling wave cases at $c < -8.64$ with $a = 0.1$ and $k = 1$.

The torque reduction is obtained when the wave travels in the co-rotating and counter rotating direction for the inner and outer cylinder controls, respectively. Four parameter sets are chosen, as the reference cases for a detailed discussion, and tabulated in Table 3: Cases 1 and 2 are the inner cylinder

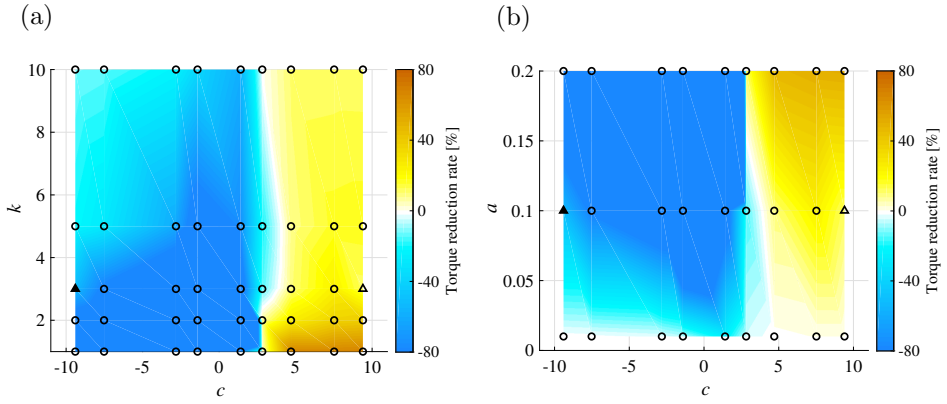

Figure 6: Map of R_T by the inner cylinder control as a function of control parameters: (a) for c and k at $a = 0.1$ and (b) for c and a at $k = 3$. Each circle represents a single simulation: filled triangle, Case 1; opened triangle, Case 2.

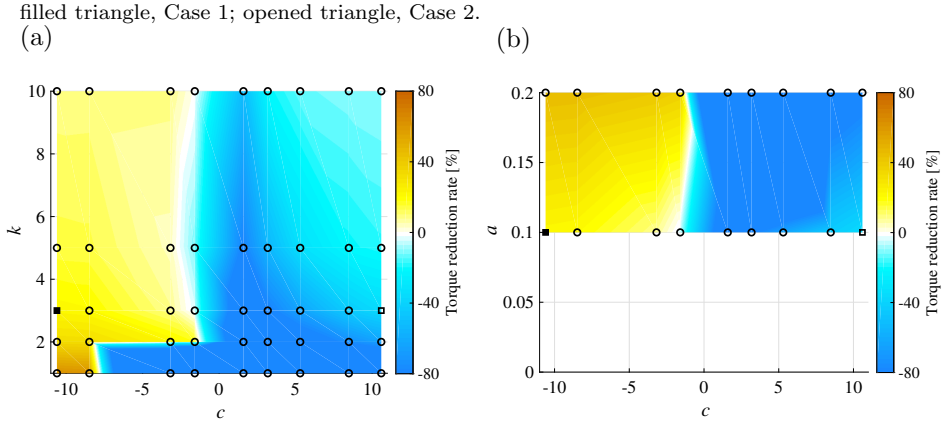

Figure 7: Map of R_T by the outer cylinder control as a function of control parameters: (a) for c and k at $a = 0.1$ and (b) for c and a at $k = 3$. Each circle represents a single simulation: filled square, Case 3; opened square, Case 4.

control while Cases 3 and 4 are the outer cylinder control. In Cases 1 and 2 (and Cases 3 and 4), the wave speed c varies, while the other parameters stay the same. Although the relaminarization phenomenon occurs in the small wavenumber cases (i.e., $k = 1$), four parameter sets at $k = 3$ are chosen to discuss an interaction between the traveling wave and the turbulent flow field. Relaminarization mechanisms will be investigated in detail in another paper.

Table 3: Parameter sets of reference cases.

	Control input	a	k	c	T	R_T
NC	–	–	–	–	5.7×10^7	–
Case 1	Inner wall	0.1	3	-9.4	7.8×10^7	-52%
Case 2	Inner wall	0.1	3	9.4	3.8×10^7	27%
Case 3	Outer wall	0.1	3	-10.6	4.2×10^7	20%
Case 4	Outer wall	0.1	3	10.6	7.1×10^7	-36%

Flow statistics in Cases 1 and 2 are shown in Fig. 8. The controlled cases are shown by the solid lines and the uncontrolled case is shown by the dashed line. As compared with the uncontrolled case, the mean azimuthal velocity increases and decreases in Cases 1 and 2 as shown in Fig. 8(a) and (b), respectively. The rms values of the velocities $\left(u_{i,\mathrm{rms}} = \sqrt{\overline{(u_i')^2}}\right)$ are shown in Fig. 8(c) and (d) and all components increase as compared with the uncontrolled case, except for $u_{z,\mathrm{rms}}$ of Case 2. As discussed later, the traveling wave creates a flow acceleration and deceleration and the rms values of the velocities are affected by them. The rms value of the azimuthal velocity $u_{\theta,\mathrm{rms}}$ in both cases significantly increase as compared with the uncontrolled case: a large peak appears in Case 1 in the region near the inner wall; $u_{\theta,\mathrm{rms}}$ is a plateau in Case 2. The non-zero value of $u_{z,\mathrm{rms}}$ that appears on the inner cylinder wall corresponds to the blowing and suction velocities. In contrast with Case 1, $u_{z,\mathrm{rms}}$ of Case 2 is found to decrease compared with the uncontrolled case. The axial velocity component $u_{z,\mathrm{rms}}$ is affected by the blowing and suction, while the variation is smaller than those of the azimuthal and wall-normal components. Figure 8(e) and (f) shows the Reynolds shear stress (referred as the RSS, hereafter). In Case 1, the RSS increases and peaks close to the inner cylinder. The peak is created by the traveling wave. In Case 2, in contrast, the RSS decreases, which results in a torque reduction. Figure 9 shows the statistics in Cases 3 and 4. While the control is imposed in the outer cylinder wall, a similar variation with the inner cylinder control is observed.

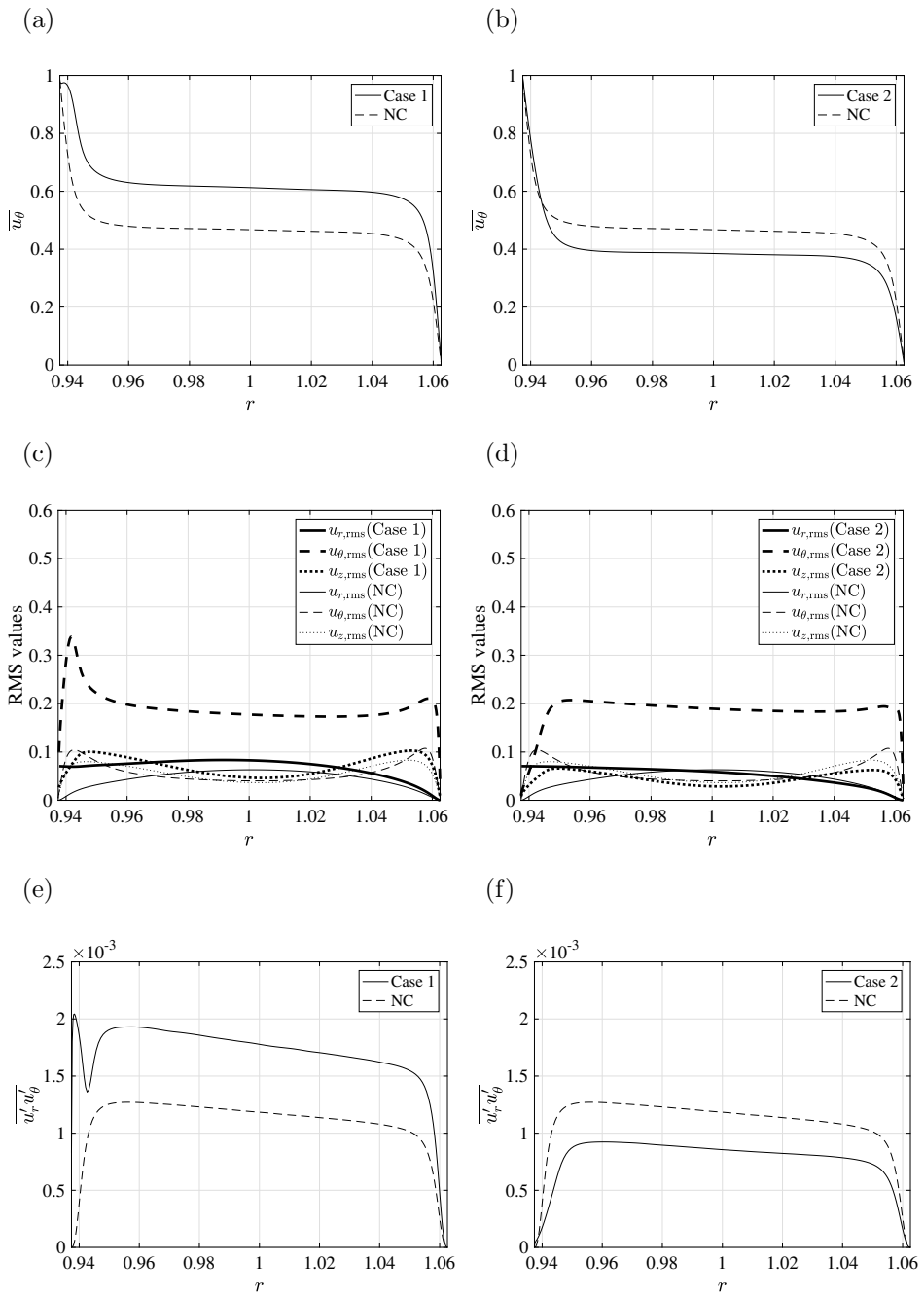

Figure 8: Flow statistics of the inner cylinder control: top, mean azimuthal velocity; middle, rms value of the velocities (blue, azimuthal velocity; black, wall-normal velocity; red, axial velocity); bottom, Reynolds shear stress. Left column, Case 1; right column, Case 2.

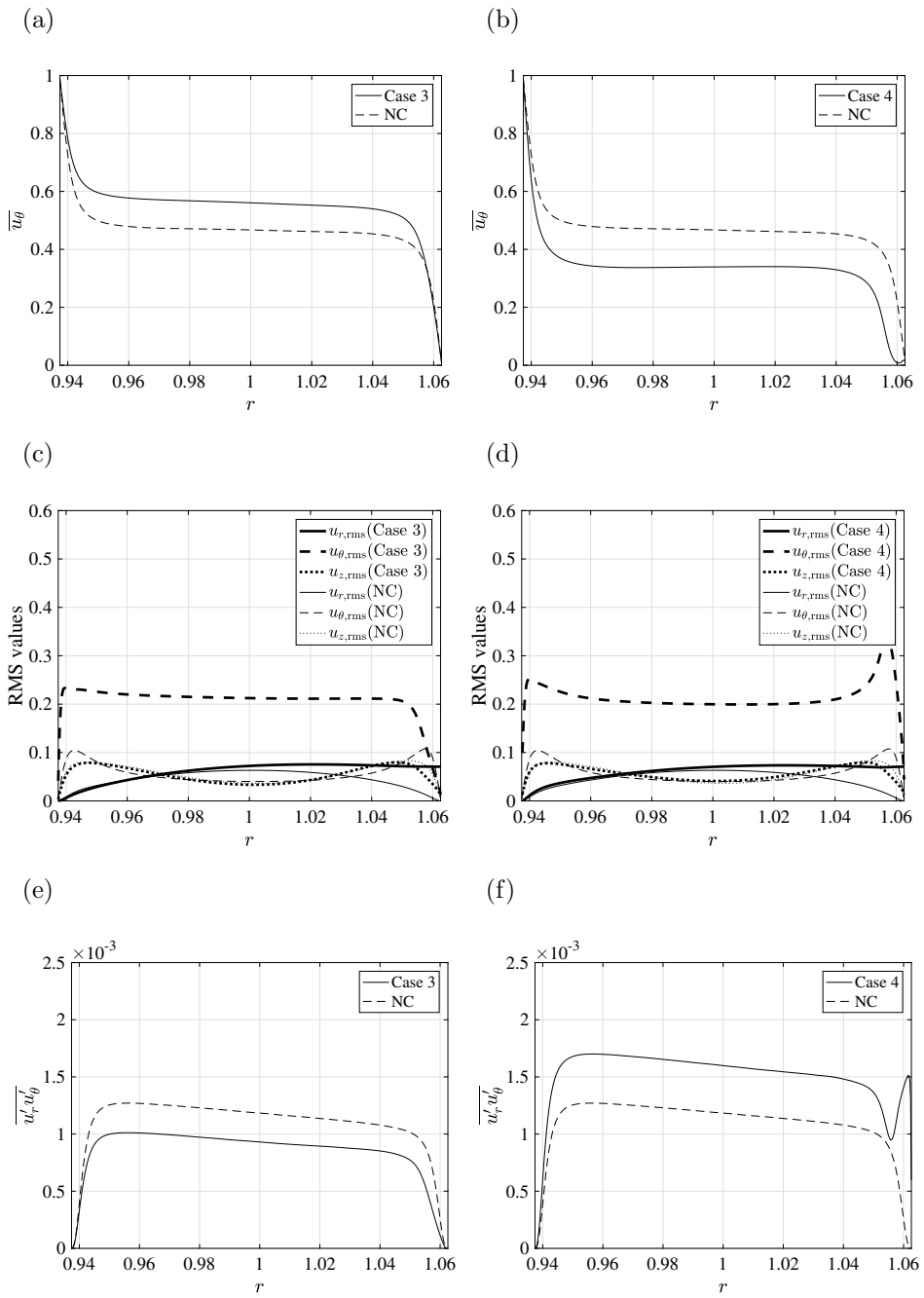

Figure 9: Flow statistics of the outer cylinder control: top, mean azimuthal velocity; middle, rms value of the velocities (blue, azimuthal velocity; black, wall-normal velocity; red, axial velocity); bottom, Reynolds shear stress. Left column, Case 3; right column, Case 4.

(a) Uncontrolled flow (b) A-A plane (c) B-B plane

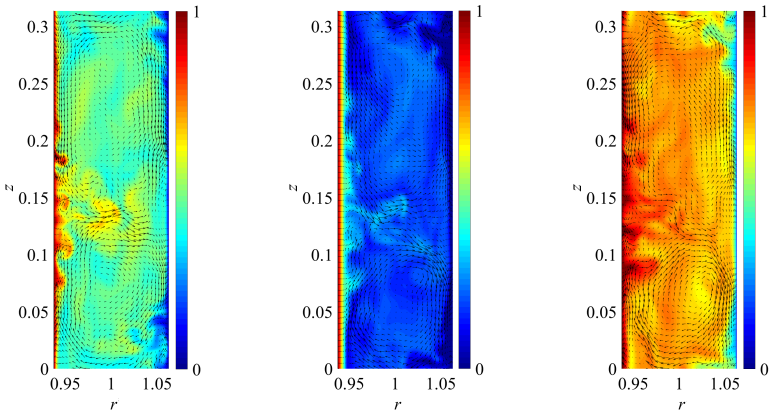

Figure 10: Instantaneous flow field on the r-z plane of the uncontrolled flow, Case 2. The color shows the azimuthal velocity and the arrows are the velocity vectors on the r-z plane. (a) Uncontrolled case; (b) and (c) are the "A-A" and "B-B" planes in Fig. 3(a).

Figure 10 shows the instantaneous flow fields. The color shows u_θ with velocity vectors on the r-z plane. In the uncontrolled case, a pair of the large vortical structures (i.e., the Taylor vortex) is observed: the "upward flow" from the inner cylinder to the outer cylinder is observed at $z \approx 0.12$; the "downward flow" is observed $z \approx 0.3$ and 0. (Note that the region is continuous due to the periodic condition in the z-direction.) The instantaneous flow fields in Case 2 are shown in Fig. 10(b) and (c). The flow is visualized on the A-A and B-B planes in Fig. 3(a): the A-A plane is the interface from the blowing to the suction part and the B-B plane is the interface from the suction to the blowing part. The combination of blowing and suction reduces u_θ on the A-A plane and increases u_θ on the B-B plane. A pair of Taylor vortices still remains, which indicates that the Taylor vortex is not directly affected by the traveling wave.

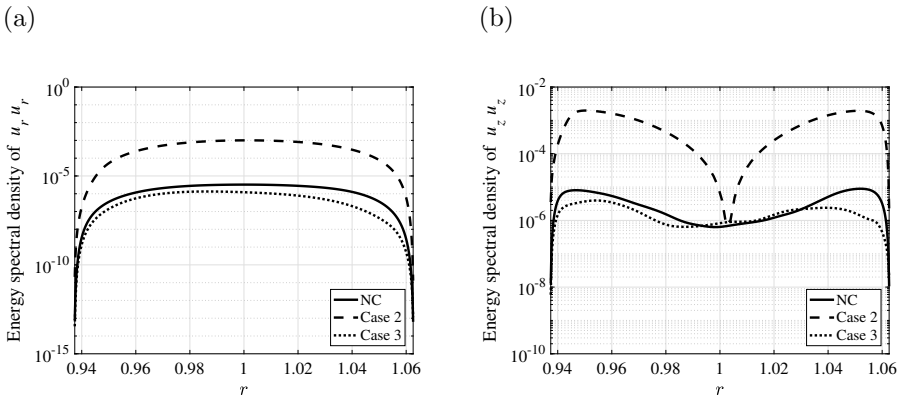

Figure 11: First mode of the energy spectral density of $u_r u_r$ and $u_z u_z$ as a function of r.

To discuss the influence of the Taylor vortex by the traveling wave control, the spectral analysis for velocity is made. Since one pair of the Taylor vortex is observed, it has the scale of L_z in the z-direction. Figure 11 shows the power spectral density of $u_r u_r$ and $u_z u_z$ components of $k_z = 2\pi/L_z$ as a function of r. The mode corresponds the Taylor vortex. In Case 2, while the drag reduction effect is obtained by the inner cylinder control, the profile is larger than that of the uncontrolled case and the Taylor vortex is enhanced. On the other hand, in Case 3, where the drag increases by the outer cylinder control, the Taylor vortex is slightly weakened.

The contribution to the torque is analyzed by the identity equation [34], as

$$c_M = \int_{R_i}^{R_o} \left(r^2 \overline{u'_\theta u'_r} - \frac{1}{\mathrm{Re}_c} r^3 \frac{\partial}{\partial r} \left(\frac{\overline{u_\theta}}{r} \right) \right) dr, \tag{6}$$

where c_M is the coefficient of the torque. The first term on the RHS of Eq. (6) is the contribution of turbulence, and the second term is that of molecular viscosity. Because the present control has a periodicity in the azimuthal direction, the three-component decomposition [7] can be applied. A phase average for an arbitrary f is defined as

$$\langle f \rangle (\phi_\theta, r) = \frac{1}{k} \sum_{\theta \in \phi_\theta} \left[\frac{1}{\mathscr{T} L_z} \int_0^{L_z} \int_0^{\mathscr{T}} f(r, \theta, z, t) dt dz \right], \tag{7}$$

with $\phi_\theta = k(\theta - ct) - 2\pi n$ $(0 < \phi_\theta < 2\pi, n \in \mathbb{Z})$ being the wave coordinate in the azimuthal direction. The $\overline{f}$ is identical to $\langle f \rangle (\phi_\theta, r)$ averaged in the azimuthal direction, as

$$\frac{1}{2\pi} \int_0^{2\pi} \langle f \rangle (\phi_\theta, r) d\phi_\theta. \tag{8}$$

The coherent component $\tilde{f}$ is defined as

$$\tilde{f}(\phi_\theta, r) = \langle f \rangle (\phi_\theta, r) - \overline{f}. \tag{9}$$

Accordingly, f can be decomposed as

$$f = \overline{f} + f' = \overline{f} + \tilde{f} + f'', \tag{10}$$

and the RSS can be decomposed as

$$\overline{u'_\theta u'_r} = \widetilde{\widetilde{u_\theta}\widetilde{u_r}} + \overline{u''_\theta u''_r}. \tag{11}$$

The first and second terms are the coherent and random RSS, respectively. Equation (11) is substituted in Eq. (6), as

$$c_M = \int_{R_i}^{R_o} \left(r^2 \widetilde{\widetilde{u_\theta}\widetilde{u_r}} + r^2 \overline{u''_\theta u''_r} - \frac{1}{\mathrm{Re}_c} r^3 \frac{\partial}{\partial r} \left(\frac{\overline{u_\theta}}{r} \right) \right) dr, \tag{12}$$

The first and second terms of the RHS of Eq. (12) are the coherent and random contributions, respectively.

Each contribution is shown in Fig. 12. In the uncontrolled case, the random contribution is a major factor for the total torque. In Cases 2 and 3, the random contribution decreases, the positive coherent contribution appears, and the molecular viscosity term is unchanged. The decrement of the random component of Case 3, in the uncontrolled case, is smaller than that of Case 2.

Figure 13 shows the decomposed RSS in Cases 2 and 3. The random-RSS decreases and the coherent-RSS appears. The small peak of the coherent-RSS appears in the region close to the inner cylinder wall in Case 2 and the outer cylinder wall in Case 3. Compared to the uncontrolled case, the RSS profiles are different from those in the controlled Poiseuille flow [2]: when the traveling wave-like blowing and suction travels in the upstream direction, the wave creates the

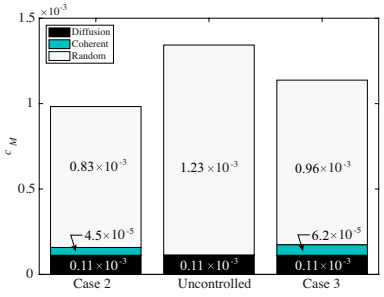

Figure 12: Contribution to c_M in Cases 2 and 3.

(a) (b)

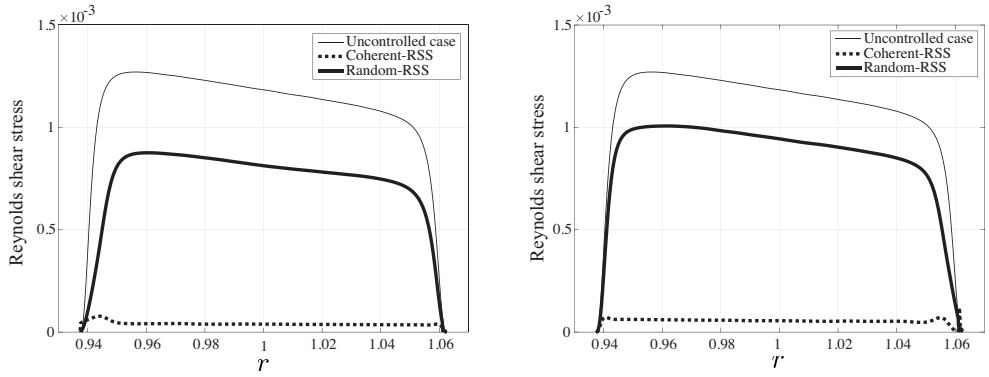

Figure 13: Decomposed RSS in Case 2 (a) and Case 3 (b).

negative coherent-RSS and the random-RSS remains, therefore the shear stress is balanced. In the TC flow, in contrast, the random-RSS decreases, whereas the coherent-RSS appears, however, it is positive.

Figure 14(a) shows the product of the coherent-velocities ($\widetilde{u_\theta}\widetilde{u_r}$) for Case 2 with vectors of mean velocities. The horizontal axis is the θ-coordinate: the maximum is $2/3\pi$ because k equals 3. The red line on the outside of the contour plot is the blowing and suction from the wall. The rotation direction of the inner cylinder corresponds to the positive θ-direction on "the bottom wall." The base flow is accelerated in the region over the blowing part, from the inner wall, and is decelerated over the suction part. Positive and negative regions are alternately distributed in the θ-direction. The positive region is slightly wider than the

(a) $\widetilde{u_\theta}\widetilde{u_r}$

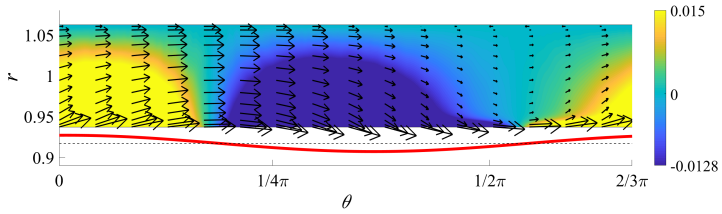

(b) $\langle u_\theta'' u_r'' \rangle$

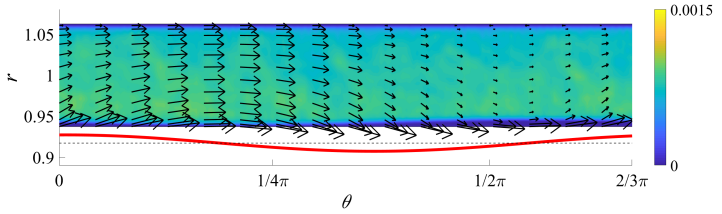

(c) $\widetilde{u_\theta}\widetilde{u_r}$

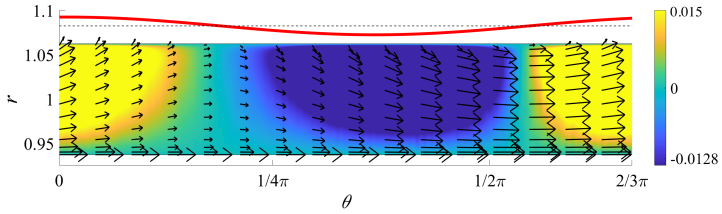

(d) $\langle u_\theta'' u_r'' \rangle$

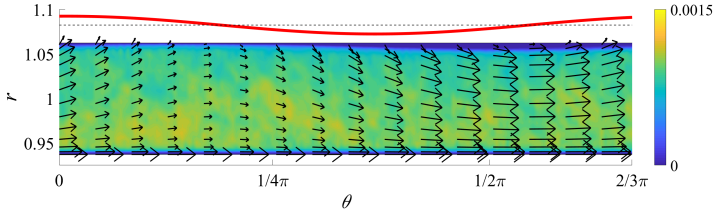

Figure 14: Distribution of coherent and random components: (a) and (b), Case 2; (c) and (d), Case 3.

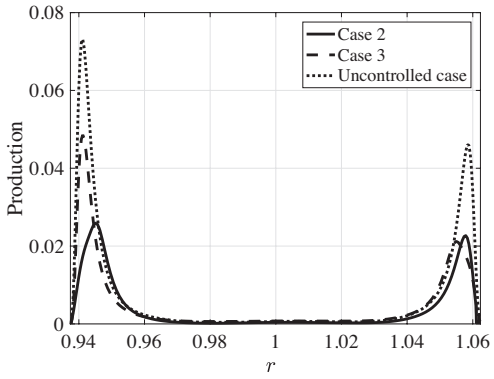

Figure 15: Production term of $\overline{u''_\theta u''_\theta}$ in Cases 2 and 3.

negative region, which results in the positive $\overline{\widetilde{u_\theta}\widetilde{u_r}}$. Figure 14(b) shows the product of random component (i.e., $u''_\theta u''_r$). The random component is mostly positive, the small region slightly thickens over the blowing part of the control. Figure 14(c-d) shows the coherent and random components in Case 3. A similar distribution to Case 2 is observed: there is a positive and negative alternation on the distribution of the coherent component, while the random component is mostly positive.

In both cases, while the traveling wave is applied on the inner or outer cylinder walls, the velocity is affected not only in the vicinity of the wall but also in the whole region. The traveling wave is characterized by a "pumping effect" [35] and the wave creates mean flux. In Cases 2 and 3, the wave creates the mean flux in the θ-direction which helps the rotation of the inner cylinder and results in a torque reduction. Furthermore, the turbulence remains and the relaminarization phenomenon, which can be observed in the Pouseuille flow [7], does not occur in the reference cases.

Figure 15 shows the production term of $\overline{u''_\theta u''_\theta}$ for Cases 2 and 3. The production term reads,

$$\text{Prod.} = -2\overline{\langle u''_\theta u''_r \rangle \frac{\partial \langle u_\theta \rangle}{\partial r}} \tag{13}$$

The production term is reduced in the controlled cases as compared to the

uncontrolled case and it results in the reduction of the random component.

4. Conclusion

The direct numerical simulation (DNS) of Taylor–Couette flow controlled by the traveling wave-like blowing and suction was performed. The parametric study reveals the influence of the control parameters on the drag reduction effect. A torque reduction is obtained when the wave on the inner cylinder travels along the co-rotating direction of the inner cylinder or the wave on the outer cylinder travels along the counter-rotating direction. For the torque reduction case, the turbulence remains and the relaminarization phenomenon does not occur at $k < 2$. The Reynolds shear stress is decreased below that of the uncontrolled case: the turbulent contribution is decreased, while the coherent component appears. The production term of the turbulence is reduced. In addition, for the faster wavespeed cases with the small wavenumber, the large torque reduction is obtained and the relaminarization phenomenon occurs in these parameter sets. Relaminarization mechanisms will be investigated in detail in another paper.

Acknowledgments

This research was partially supported by the Ministry of Education, Culture, Sports, Science, and Technology through a Grant-in-Aid for Young Scientists (B) of JP16K18019 in 2017.

[1] K. Fukagata, K. Iwamoto, N. Kasagi, Contribution of Reynolds stress distribution to the skin friction in wall-bounded flows, Physics of Fluids 14 (2002) L73–L76.

[2] T. Min, S. M. Kang, J. L. Speyer, J. Kim, Sustained sub-laminar drag in a fully developed channel flow, Journal of Fluid Mechanics 558 (2006) 309–318.

[3] C. Lee, T. Min, J. Kim, Stability of a channel flow subject to wall blowing and suction in the form of a traveling wave, Physics of Fluids 20 (2008) 101513, 8 pp.

[4] R. Moarref, M. R. Jovanović, Controlling the onset of turbulence by streamwise travelling waves. Part 1. Receptivity analysis, Journal of Fluid Mechanics 663 (2010) 70–99.

[5] B. K. Lieu, R. Moarref, M. R. Jovanović, Controlling the onset of turbulence by streamwise travelling waves. Part 2. Direct numerical simulation, Journal of Fluid Mechanics 663 (2010) 100–119.

[6] R. Nakanishi, H. Mamori, K. Fukagata, Relaminarization of turbulent channel flow using traveling wave-like wall deformation, International Journal of Heat and Fluid Flow 35 (2012) 152–159.

[7] H. Mamori, K. Iwamoto, A. Murata, Effect of the parameters of traveling waves created by blowing and suction on the relaminarization phenomena in fully developed turbulent channel flow, Physics of Fluids 26 (2014) 015101, 15 pp.

[8] K. Higashi, H. Mamori, K. Fukagata, Simultaneous control of friction drag reduction and heat transfer argumentation by traveling wave-like blowing/suction, Computational Thermal Sciences 3 (2011) 521–530.

[9] K. Uchino, H. Mamori, K. Fukagata, Heat transfer in fully developed turbulent channel flow with streamwise traveling wave-like wall deformation, Journal of Thermal Science and Technology 12 (2017) Paper No.16–00624, 11 pp.

[10] F. Xu, W. F. Bai, W. L. Chen, Y. Q. Xiao, J. P. Ou, Flow control on the vortex-induced vibration of a circular cylinder using a traveling wave wall method, Advances in Structural Engineering 21 (2018) 1664–1675.

[11] G. I. Taylor, VIII. Stability of a viscous liquid contained between two rotating cylinders, Philosophical Transactions of the Royal Society of London.

Series A, Containing Papers of a Mathematical or Physical Character 223 (1923) 289 LP – 343.

[12] C. D. Andereck, S. S. Liu, H. L. Swinney, Flow regimes in a circular Couette system with independently rotating cylinders, Journal of Fluid Mechanics 164 (1986) 155–183.

[13] D. Coles, Transition in circular Couette flow, Journal of Fluid Mechanics 21 (1965) 385–425.

[14] P. R. Fenstermacher, H. L. Swinney, J. P. Gollub, Dynamical instabilities and the transition to chaotic Taylor vortex flow, Journal of Fluid Mechanics 94 (1979) 103–128.

[15] D. Lathrop, J. Fineberg, H. Swinney, Transition to shear-driven turbulence in Couette-Taylor flow, Physical Review A 46 (1992) 6390–6404.

[16] D. P. Lathrop, J. Fineberg, H. L. Swinney, Turbulent flow between concentric rotating cylinders at large Reynolds number, Physical Review Letters 68 (1992) 1515–1518.

[17] Y. Takeda, Quasi-periodic state and transition to turbulence in a rotating Couette system, Journal of Fluid Mechanics 389 (1999) 81–99.

[18] L. Wang, M. G. Olsen, R. D. Vigil, Reappearance of azimuthal waves in turbulent Taylor-Couette flow at large aspect ratio, Chemical Engineering Science 60 (2005) 5555–5568.

[19] G. S. Lewis, H. L. Swinney, Velocity structure functions, scaling, and transitions in high-Reynolds-number Couette-Taylor flow, Physical Review E - Statistical Physics, Plasmas, Fluids, and Related Interdisciplinary Topics 59 (1999) 5457–5467.

[20] A. Racina, M. Kind, Specific power input and local micromixing times in turbulent Taylor-Couette flow, Experiments in Fluids 41 (2006) 513–522.

[21] M. Bilson, K. Bremhorst, Direct numerical simulation of turbulent Taylor–Couette flow, Journal of Fluid Mechanics 579 (2007) 227–270.

[22] S. Dong, Direct numerical simulation of turbulent Taylor - Couette flow, Journal of Fluid Mechanics 587 (2007) 373–393.

[23] D. Pirrò, M. Quadrio, Direct numerical simulation of turbulent Taylor-Couette flow, European Journal of Mechanics, B/Fluids 27 (2008) 552–566.

[24] W. He, M. Tanahashi, T. Miyauchi, Direct numerical simulation of turbulent Taylor-Couette flow with high Reynolds number, in: European Turbulence Conference, 2007, p. 11 pp.

[25] K. Osawa, Y. Naka, N. Fukushima, M. Shimura, M. Tanahashi, T. Miyauchi, Effect of Flow Structures on Turbulence Statistics of Taylor-Couette Flow in the Torque Transition State, Flow, Turbulence and Combustion 97 (2016) 973–986.

[26] N. Fukushima, T. Fushimi, M. Shimura, M. Tanahashi, T. Miyauchi, Dynamics of large– and small–scale vortical structures in turbulent Taylor–Couette flow, in: Turbulent Shear Flow Phenomena 7, 2011, pp. Paper No. 9B2P, 6 pp.

[27] K. Avila, B. Hof, High-precision Taylor-Couette experiment to study subcritical transitions and the role of boundary conditions and size effects, Phys. Fluids 065106 (2013).

[28] S. Grossmann, D. Lohse, C. Sun, High–Reynolds Number Taylor-Couette Turbulence, Annual Review of Fluid Mechanics 48 (2016) 53–80.

[29] K. Watanabe, T. Akino, Drag Reduction in Laminar Flow Between Two Vertical Coaxial Cylinders, Journal of Fluids Engineering 121 (2016) 541–547.

[30] A. J. Greidanus, R. Delfos, S. Tokgoz, J. Westerweel, Turbulent Taylor–Couette flow over riblets: drag reduction and the effect of bulk fluid rotation, Experiments in Fluids 56 (2015) 13 pp.

[31] C. Le Dauphin, K. Fukagata, Opposition control of turbulent Taylor-Couette flow, in: ASME-JSME-KSME Joint Fluids Engineering Conf. 2011 (AJK2011), Proc. ASME-JSME-KSME Joint Fluids Engineering Conf. 2011 (AJK2011), Hamamatsu, Japan, 2011, p. 9 pp.

[32] H. Choi, P. Moin, J. Kim, Active turbulence control for drag reduction in wall-bounded flows, Journal of Fluid Mechanics 262 (1994) 75–110.

[33] K. Fukagata, N. Kasagi, Highly energy-conservative finite difference method for the cylindrical coordinate system, Journal of Computational Physics 181 (2002) 478–498.

[34] A. Ohsawa, A. Murata, K. Iwamoto, Contribution of advetion, turbulent transport and diffusion terms to Nusselt number and torque coefficient in Taylor-Couette flow, Journal of Thermal Science and Technology 11 (2016) Paper No.16–00350, 13 pp.

[35] J. Hœpffner, K. Fukagata, Pumping or drag reduction?, Journal of Fluid Mechanics 635 (2009) 171–187.

Nomenclature

α	scaling exponent
δ	half width of the gap
$\mathscr{T}$	averaging time
Re	Reynolds number
$-\overline{u'v'}$	Reynolds shear stress of channel flow
ξ	ratio between the inner and outer cylinder radii
*	dimensional variable
a	amplitude of the wave
c	wavespeed
c_f	Skin-friction drag coefficient
c_M	coefficient of the torque
f	arbitrary
G	dimensionless toque
k	wavenumber
L_z	Computational domain in axial direction
N_θ	Number of computational grid points in azimuthal direction
N_r	Number of computational grid points in wall-normal direction
N_z	Number of computational grid points in axial direction
R_c	location of centerline between two cylinders
R_i	inner cylinder radius
R_o	outer cylinder radius

R_T	torque reduction rate
T	torque
u_θ	azimuthal velocity
$u'_\theta u'_r$	Reynolds shear stress
u_r	wall-normal velocity
U_w	wall velocity of inner cylinder
u_z	axial velocity
$u_{r,w}$	wall-normal velocity on the wall
y	wall-normal coordinate